



# Experimental study on seismic behavior of recycled aggregate concrete infilled profile steel structures

Jian Liu<sup>1</sup> · Qinpeng Yang<sup>1</sup>

Received: 19 December 2023 / Accepted: 29 February 2024 / Published online: 28 March 2024  
© The Author(s), under exclusive licence to The Brazilian Society of Mechanical Sciences and Engineering 2024

## Abstract

To alleviate the shortage of river sand and the pollution of construction waste, this paper proposed the recycled aggregate concrete (RAC) and its application in structures. Two specimens at 1:2 scale are tested under quasi-static cyclic load, and the results were verified by the finite element model (FEM). The specimen KJ-1 is a frame structure composed of the steel tube column with RAC infilled profile steel and the H-shaped steel beam, and the specimen KJ-W is a frame-shear wall structure composed of the steel tube column with RAC infilled profile steel, the H-shaped steel beam and reinforced concrete shear wall. The failure mode of the specimens is presented. Based on the experimental data, the hysteresis curves, skeleton curves, ductility, energy dissipation capacity, and stiffness degradation of the specimens are analyzed. The difference of peak bearing capacity of specimens with different RAC structures is 15.2%. The ductility coefficient of the KJ-W increased by 7.4% compared with the KJ-1. The KJ-W shows worse coordinate performance with the frame after the cracking of reinforced concrete shear wall, while in the KJ-1, the steel tube column with RAC infilled profile steel can effectively resist horizontal load, which can protect the specimen from stiffness degradation in a relatively slow speed.

**Keywords** Recycled aggregate concrete · Quasi-static cyclic test · Seismic behavior

## 1 Introduction

The reuse of RAC has emerged as a prominent focal point in recent academic research. Presently, countries such as the United States, Japan, and European countries have primarily concentrated their efforts on the utilization of the fundamental properties of RAC, such as physical characteristics, mechanical behavior, work performance and durability [1–5]. Due to the significant difference observed in RAC, scholars from different regions have arrived at varying conclusions in their research [6–8].

Currently, the practical application of RAC in engineering projects in China remains relatively limited, with only a few examples of its utilization [9, 10]. This significantly constrains the application and development of RAC technology. Nevertheless, steel tube concrete structures combine

the advantages of both steel tubes and concrete materials, offering high structural load-bearing capacity and excellent seismic performance [11–14]. This architectural structural form is widely adopted today. Scholars have integrated the distinctive features of steel tubes and recycled concrete and introduced the concept of RAC infilled steel tube composite structures [15–18]. This concept involves using an external steel tube to confine the RAC, enhancing the structural load-bearing performance of RAC structures and improving the ductility and seismic performance of typical recycled concrete structures [19]. However, current research on steel tube recycled concrete predominantly focuses on the structural member (eg. a single column or beam) [20], with relatively limited investigation into its entire structure. In contrast to structural members, the structure behavior of steel tube RAC is more complicated. Since reference [21–23] has already conducted research on the seismic performance of this type of structure with ordinary concrete, this manuscript mainly explores the seismic performance of these two types of structures with RAC.

This is particularly evident in the frame and concrete core tube structure, the few available experiments to specific engineering projects, limiting their applicability as general

---

Technical Editor: Ehsan Noroozinejad Farsangi.

✉ Qinpeng Yang  
yangqinpeng@e.gzhu.edu.cn

<sup>1</sup> School of Civil Engineering, Guangzhou University, Guangzhou 510006, People's Republic of China

guidelines. Furthermore, there are limited reference materials on its seismic performance, influencing factors, as well as the mechanisms of structural seismic damage. A flow-chart illustrating the stages of our research work is shown in Fig. 1.

## 2 Experimental design

### 2.1 Experiment specimens design

The prototype structure of the experiment specimens are shown in Fig. 2. In the experiments, the KJ-1 and the KJ-W specimens are a ratio of 1:2 scale of prototype structure. Both specimens are designed according to Code for Design of Concrete Structures (GB 50010–2010) [24] and Code for Design of Composite Structures (JGJ138-2016) [25]. Specific parameters and geometric dimensions of each specimens are detailed in Figs. 3 and 4. Specifically, the specimen KJ-1 is a frame structure composed of the steel tube column with RAC infilled profile steel and the H-shaped steel beam, and the specimen KJ-W is a frame-shear wall structure composed of the steel tube column with RAC infilled profile steel, the H-shaped steel beam and reinforced concrete shear wall. For the KJ-W, the frame structure connected to reinforced concrete shear walls through the H-shaped steel beam. The dimensions of the reinforced concrete shear wall is 1500 mm × 800 mm × 100 mm, with a double-layer bidirectional arrangement of HRB400 steel bars having a diameter of 14 mm and a spacing of 200 mm. The H-shaped steel beams with double-sided angle welds between the flanges and web plates. The steel beam and steel tube column joint are achieved through external 10 mm-thick steel sleeves and 20 mm-thick steel plates using M24 high strength bolts. The steel tube columns in the specimens are made of finished electric resistance welded (ERW) steel pipes.

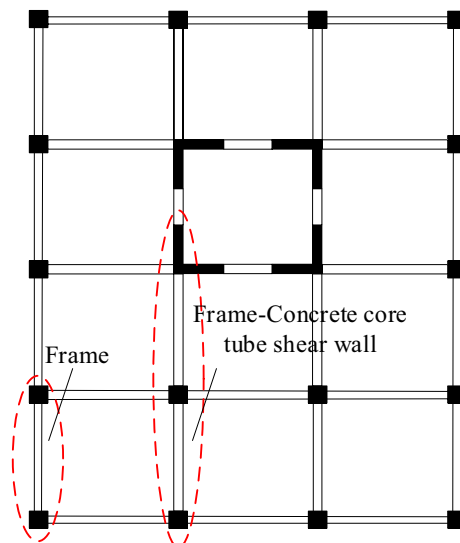


Fig. 2 Structural prototype of experiment specimens

### 2.2 Material properties

In this experiment’s frame, the replacement rate of RAC is 100% with the column. The steel strength grade is Q345, and the shear wall made from strength grade C40 of ordinary concrete. The steel materials include steel tubes (matching the steel sleeve material), steel beam, and steel plates are Q345B with a thickness of 8 mm, 10 mm, and 12 mm. The steel plate is sampled and stretched according to GB/T228.1 [26], as shown in Fig. 5. The results are listed in Table 1.

In this experiments, the recycle aggregates are screened according to GB/T 25177 [27]. After manual screening and cleaning, aggregates with a particle size of 5–25 mm are obtained. As shown in Fig. 6, the aggregates could meet the requirements of an abandoned office building stone in

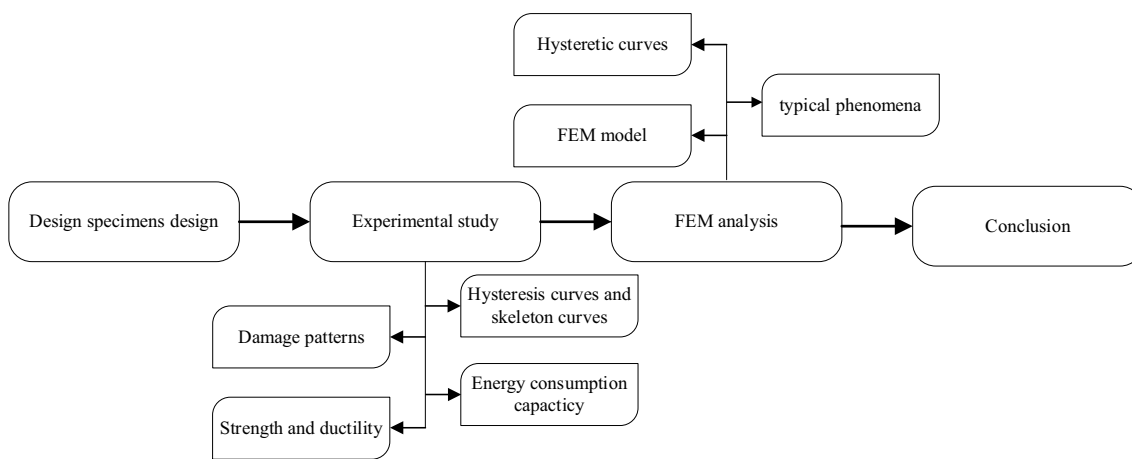
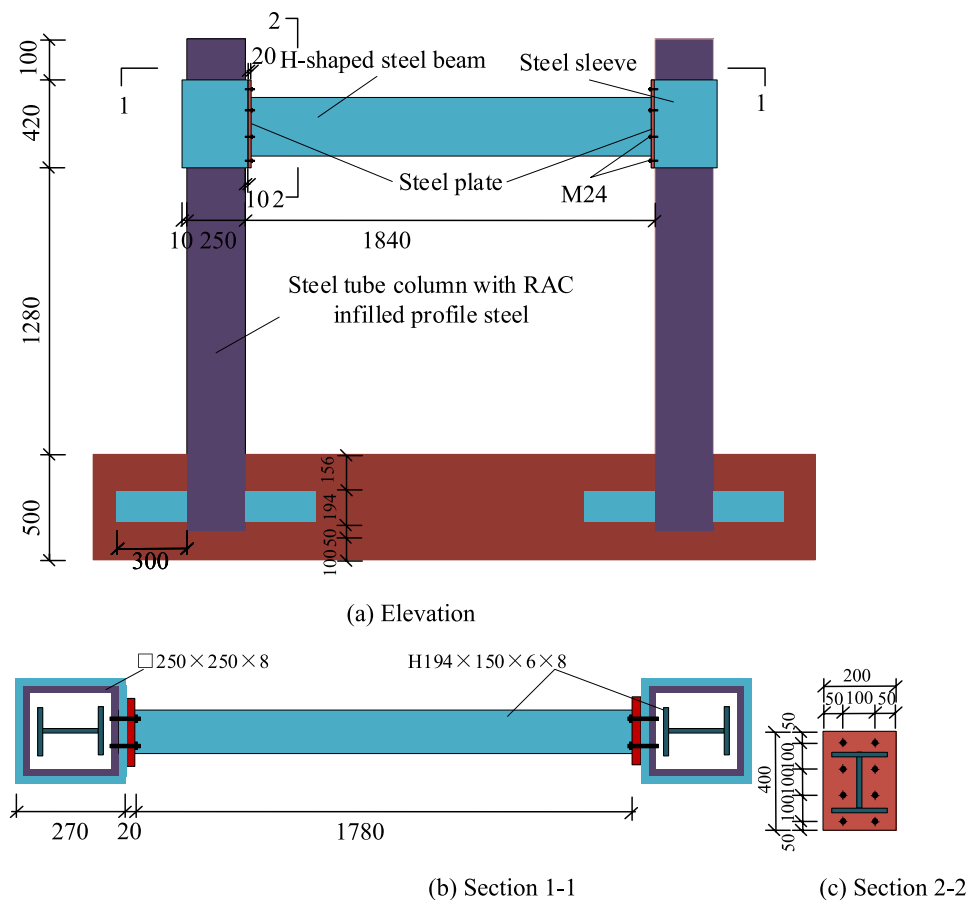


Fig. 1 Flowchart of the paper stages

**Fig. 3** Geometric dimensions of the KJ-1 (unit: mm)

Guangzhou city. Ordinary concrete uses natural sand and aggregates. The 42.5 grade ordinary Portland cement and natural sand are selected for the RAC and ordinary concrete. The mixture concrete proportion design of the RAC is according to JGJ/T443-2018 [28], as shown in Table 2. The properties experiments for the concrete specimens conducted in according to GB/T50081-2019 [29]. The material properties of concrete are presented in Table 3 and Fig. 7.

### 2.3 Experimental equipment and loading system

The experimental equipment as is illustrated in Fig. 8. The reinforced concrete foundation is fixed on the reaction beam with anchor bolts. A horizontal 50-ton hydraulic jack is employed to press the bottom beam tightly to prevent slippage during the loading process. Sliding devices are placed at the bottom of the jack and the reaction beam to eliminate the influence of friction. The MTS 30t electro-hydraulic actuator loading system is used in the experiment to carry out horizontal reciprocating loading on the specimen to simulate the effect of earthquake on the structure.

The experiment method and loading system are according to JGJ/T101 [30] for designing. The loading is using displacement control, with an initial displacement of

1.875 mm (1/800 of the drift). The subsequent level of displacement was set to 3.75 mm (1/400 of the drift), and each increment is increased by 1.5 times. Each level of displacement is cycled twice until the specimen yielded. The yield displacements of the samples could be determined by the experimental phenomenon; it is either the inflection point observed from the displacement-load curve, the yielding of the steel beam flange observed from the strain collection instrument, or the initial cracking is presented in the reinforced concrete shear wall. The yield displacements for the KJ-1 and the KJ-W are found to be 22.5 mm (1/22 of the drift) and 11.25 mm (1/44 of the drift), respectively. When the horizontal drifts is greater than 1/22 for the KJ-1 and the 1/44 for the KJ-W, each level of displacement is loaded three times. The specimens approached failure during loading: (1) the horizontal bearing capacity of the specimens is only 85% of the peak value; (2) the lower flange of the steel beam in the connection region is severely buckled or the weld is completely broken; (3) the significant overall bending of the column is observed. It is necessary to record the horizontal load and deformation data. As the failure load and deformation, the loading is terminated. The loading protocol is depicted in Fig. 9,

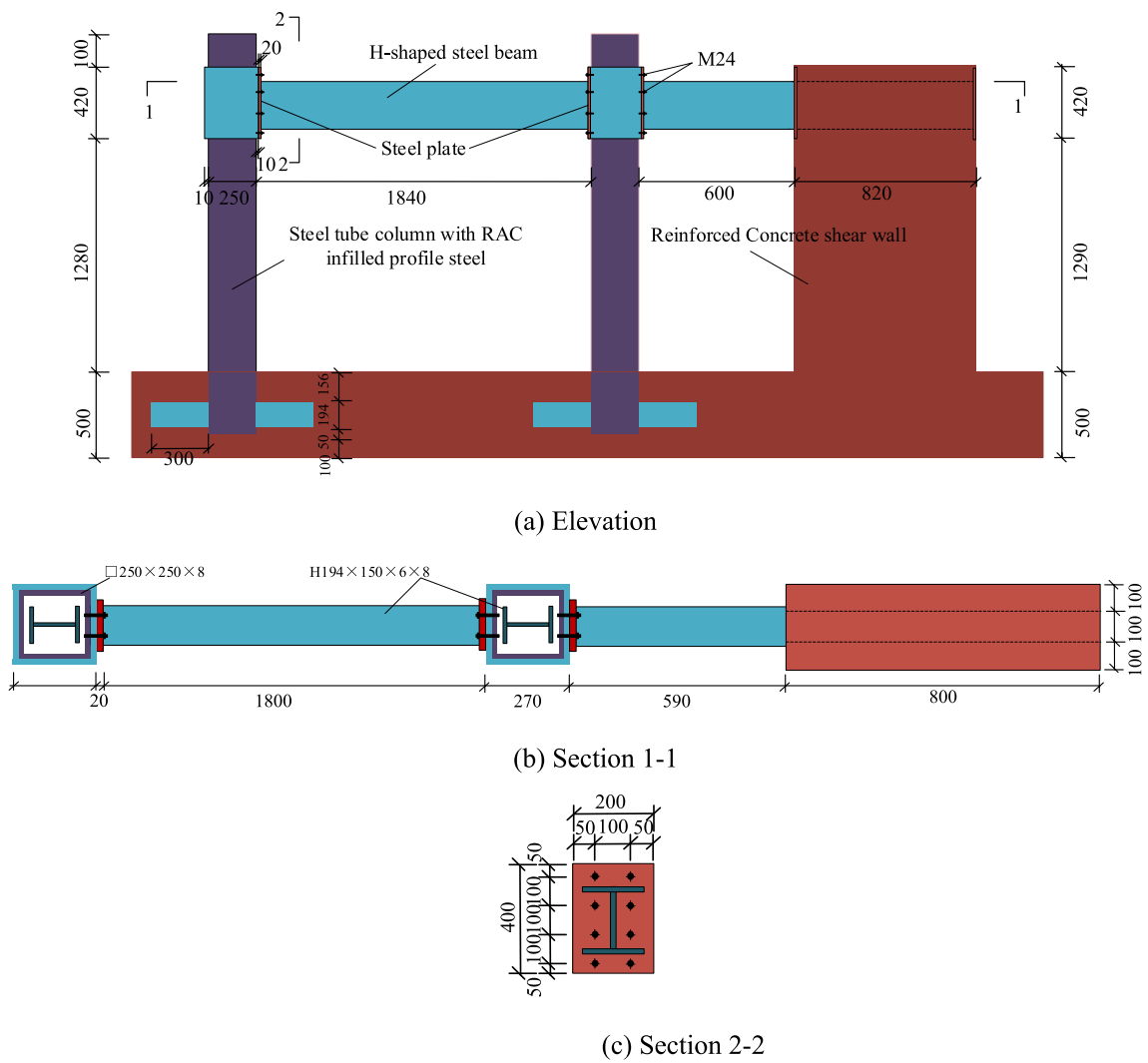


Fig. 4 Geometric dimensions of the KJ-W (unit: mm)

Fig. 5 Steel profile tensile test



**Table 1** Mechanical properties of steel

Material type	Thickness (mm)	Yield strength $f_y$ (MPa)	Yield strain $\epsilon_y$ ( $10^{-3}$ mm/mm)	Ultimate strength $f_u$ (MPa)	Elastic modulus $E_s$ (MPa)
Steel tube	10	436.3	2.098	496.9	$2.08 \times 10^5$
Profile steel	8	418.2	2.112	488.8	$1.98 \times 10^5$
Steel beam	8	426.8	2.023	491.2	$2.11 \times 10^5$
Steel plate	20	431.9	1.981	501.4	$2.18 \times 10^5$

**Fig. 6** Aggregates for RAC

with positive displacement applied for compression and negative displacement applied for tension.

## 2.4 Data collection and measurement

The experiment utilized the JM3813 multi-functional static strain testing system. Unidirectional strain gauges are affixed at a distance of 5 cm on the core area of the steel

**Table 3** Mechanical properties of concrete

Concrete	Cube strength $f_{cu}$ (MPa)	Prism strength $f_{ck}$ (MPa)	Elastic modulus $E_s$ (MPa)
RAC	45.2	35.6	$3.21 \times 10^4$
Ordinary	52.1	40.6	$3.86 \times 10^4$

**Table 2** Concrete mixture

Concrete	RAC substitution rate (%)	Cement ( $\text{kg m}^{-3}$ )	Gravel ( $\text{kg m}^{-3}$ )	Recycle aggregates ( $\text{kg m}^{-3}$ )	Sand ( $\text{kg m}^{-3}$ )	Water ( $\text{kg m}^{-3}$ )
RAC	100	443	–	1169	576	203
Ordinary	0	443	1169	–	576	184

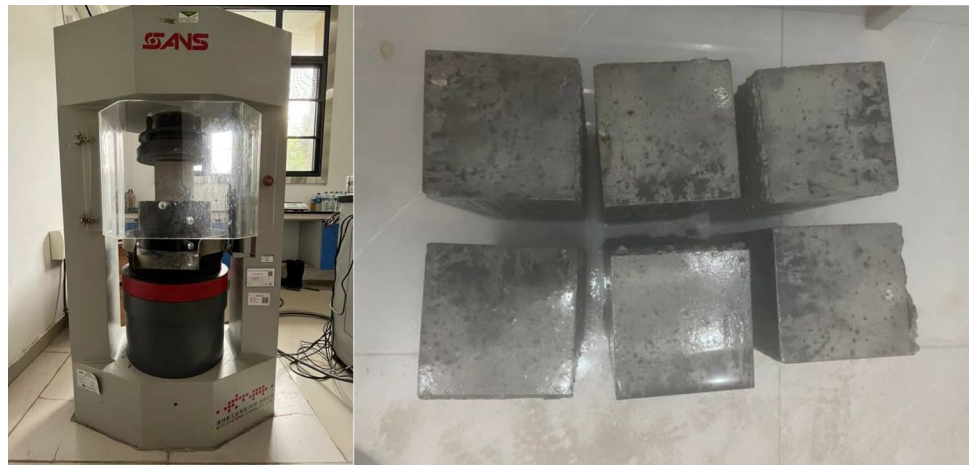
tube columns to analyze the strain distribution around the steel tubes. Strain gauges are also strategically placed on the web and flange of the steel beams to measure the strains in the beams. The three spring displacement sensors (model number YHD-10 and YHD-20) are used to measure the displacement of the column top, column center and column bottom of the KJ-1. Similarly, the three spring displacement sensors are used to measure the displacement of the column top, column center, column bottom and middle part of the shear wall of the KJ-W. Horizontal loads at the loading end and corresponding displacements are collected using the MTS 30-ton hydraulic servo actuator in the laboratory. The measuring instruments are illustrated in Fig. 10, while the arrangement of displacement sensors and strain gauge locations can be observed in Fig. 11.

## 3 Experiment results and analysis

### 3.1 Damage and failure mode

Based on the experimental results, this section primarily investigates the regions of more severe damage to the specimens and discusses the corresponding drift associated with failure modes. In the KJ-1, the regions of more severe damage are observed at the junction of the H-shaped steel beam and the steel tube column with RAC infilled profile steel, as well as at the base of the column, as shown in Figs. 12 and 13. In the KJ-W, the severely damaged regions of the junction of the H-shaped steel beam and the steel tube column with RAC infilled profile steel, the base of the column, and the reinforced concrete shear wall, as presented in Figs. 14, 15, and 16. At a drift of 1/133, there are no significant changes observed at the junction of the H-shaped steel beam and the steel tube column with RAC infilled profile steel

**Fig. 7** Material properties test of concrete



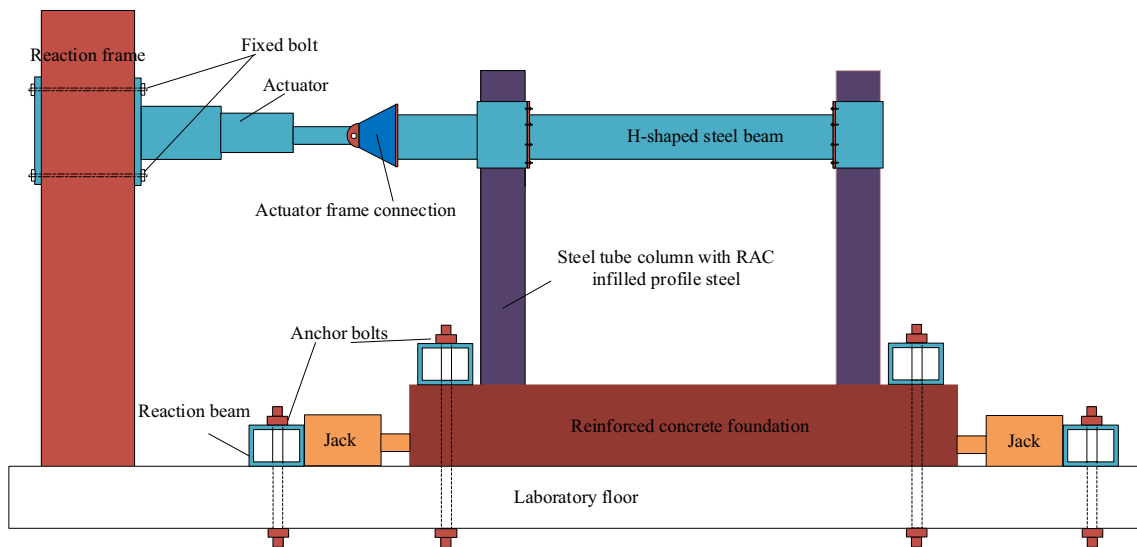
joint or at the base of the column in the KJ-W. However, minor cracks appear in the shear wall. The KJ-1 remains in the elastic undamaged stage. There are no significant changes in the KJ-W at the junction of the H-shaped steel beam and the steel tube column with RAC infilled profile steel or at the bottom of the column, but cracks in the shear wall increase in size and number, leading to the appearance of X-shaped cracks with the drift of 1/67. In the KJ-1, the lower flange of the junction of the H-shaped steel beam and the steel tube column with RAC infilled profile steel emerge slight bending, and four bolts connecting the H-shaped steel beam to the steel tube column with RAC infilled profile steel bend. Slight deformation occurred in the outer steel tube of the steel tube column with RAC infilled profile steel with the same drift of the KJ-1. There are no significant changes in the KJ-W at the junction of the H-shaped steel beam and the steel tube column with RAC infilled profile steel or at the bottom of the column, but cracks in the shear wall are increase with a drift of 1/44. At a drift of 1/33, the KJ-W shows slight bending of the upper and lower flanges of the junction of the H-shaped steel beam and the steel tube column with RAC infilled profile steel. Cracks appear at the connection between the bottom of the column and the reinforced concrete foundation, and cracks traverse through the shear wall, exposing the reinforcement. In the KJ-1, both upper and lower flanges of the junction of the H-shaped steel beam and the steel tube column with RAC infilled profile steel exhibit significant bending. The concrete at the connection between the bottom of the column and the reinforced concrete foundation starts to uplift and crack. The KJ-W is significant bending of the upper flange of the junction of the H-shaped steel beam and the steel tube column with RAC infilled profile steel and cracks at the connection between the bottom of the column and the reinforced concrete foundation increase in size at a drift of 1/27. Cracks traverse is through the shear wall and the reinforcement, indicating failure of the shear wall component, and the loading is stopped. The

KJ-1 shows pronounced bending of both the upper and lower flanges of the junction of the H-shaped steel beam and the steel tube column with RAC infilled profile steel, with a noticeable “wave-like” bending pattern. The web plate is bending as well, and the concrete at the connection between the bottom of the column and the reinforced concrete foundation continues to uplift and crack under the drift of 1/22. At a drift of 1/17, the KJ-1 exhibits significant bending and pronounced “wave” bending patterns of both the upper and lower flanges of the junction of the H-shaped steel beam and the steel tube column with RAC infilled profile steel. The web plate shows significant bending, and the concrete at the connection between the base of the column and the reinforced concrete foundation detaches, resulting in cracking. The load decreases to 85% of the peak load, indicating component failure.

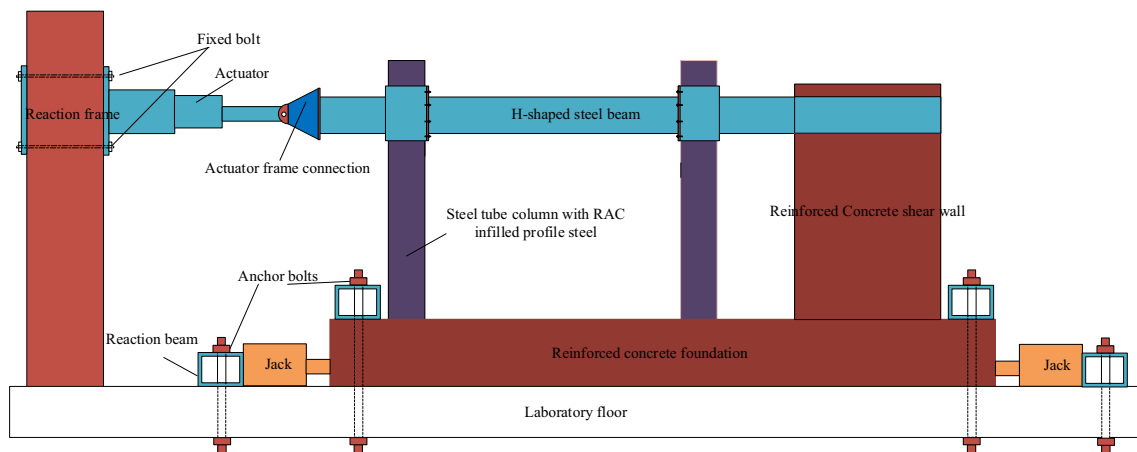
The junction of the H-shaped steel beam and the steel tube column with RAC infilled profile steel, and the bottom of the steel tube column with RAC infilled profile steel is more severe damage in the KJ-1 compared to the KJ-W, that under the same horizontal drift.

### 3.2 Strain analysis

Strain comparison is made between the KJ-1 and the KJ-W respectively under the reciprocating horizontal load. The strain of the column is depicted in Figs. 17 and 18. For both the KJ-1 and KJ-W, the strains in different regions of the steel tubes of the steel tube column with RAC infilled profile steel increased with the increasing drift. During the loading process, the steel tubes in the upper and middle sections of the column in both specimens remained in the elastic state. The steel tube strain in the lower part of the left column of the KJ-1 reached the yield strain ( $2.098 \times 10^{-3}$  mm/mm). Similarly, for both the KJ-1 and KJ-W, the steel tube strains at the column base reached the yield strain, with the largest strain observed in the bottom



(a) Load to the KJ-1



(b) Load to the KJ-W



(c) Site picture of load to the KJ-1 specimen (d) Site picture of load to the KJ-W specimen

Fig. 8 Installation and loading diagram of specimen

Fig. 9 Loading system

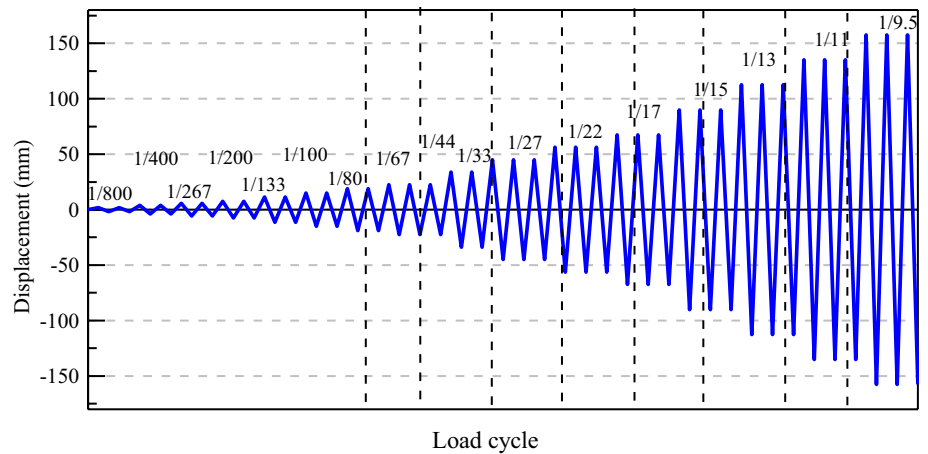
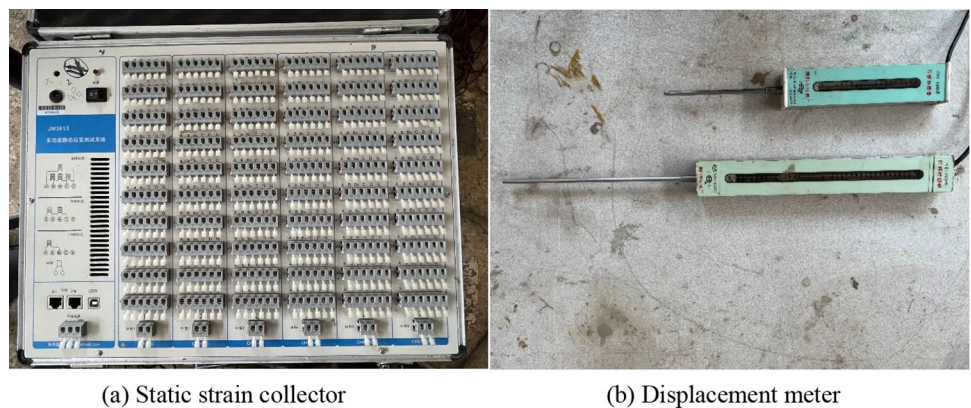


Fig. 10 Measuring instruments



(a) Static strain collector

(b) Displacement meter

region of the column. Under the same drift loading conditions, it is observed that the KJ-1 is larger strains in the steel tube column with RAC infilled profile steel compared to the KJ-W.

The strains of the steel beam between the steel tube columns with RAC infilled profile steel of both the KJ-1 and KJ-W is illustrated in Fig. 19. In both the KJ-1 and KJ-W, the strain measurements in the H-shaped steel beams increased with the increasing drift. The strains in the left and right flanges as well as the web of the steel beams reached the yield strain of the steel ( $2.023 \times 10^{-3}$  mm/mm) at the point of specimen failure. Under the same drift, the KJ-1 is larger strains in the left flange of the steel beams compared to the KJ-W. Both the KJ-1 and KJ-W increased strains in the right flange and both flanges of the steel beams, while for other drifts, the strains in these regions of the two specimens are relatively close at a drift of 1/27.

The strains in the H-shaped steel beams between the steel tube column with RAC infilled profile steel and the reinforced concrete shear wall of the KJ-W is illustrated in Fig. 20. In the KJ-W, the strain measurements in the steel beams increased with the increasing drift. Moreover, the

strains in various regions of the steel beams remained in the elastic state during the loading process.

The strains in the reinforced concrete shear wall of the KJ-W are presented in Fig. 21. The reinforced concrete shear wall exhibited severe damage during the loading process, with the appearance of fine concrete cracks at a drift of 1/133. With the drift increased, these concrete cracks further expanded. In the upper right region of the shear wall, strain gauges Q1-4 and Q1-5, as well as in the lower right region with strain gauges Q1-14 and Q1-15, showed significant displacements. The strain data collected in the regions became distorted, and therefore, they are not presented in the figure. The strains in various regions of the reinforced concrete shear wall entered the plastic state at a drift of 1/133 and continued to increase with the increasing drift until the point of failure.

### 3.3 Hysteresis curves

It can be seen from Fig. 22, the hysteretic curves and skeleton curves of the KJ-1 and the KJ-W are smooth and full shape. In the initial stage of loading, the hysteretic curves are long and narrow, the surrounding area is small and the



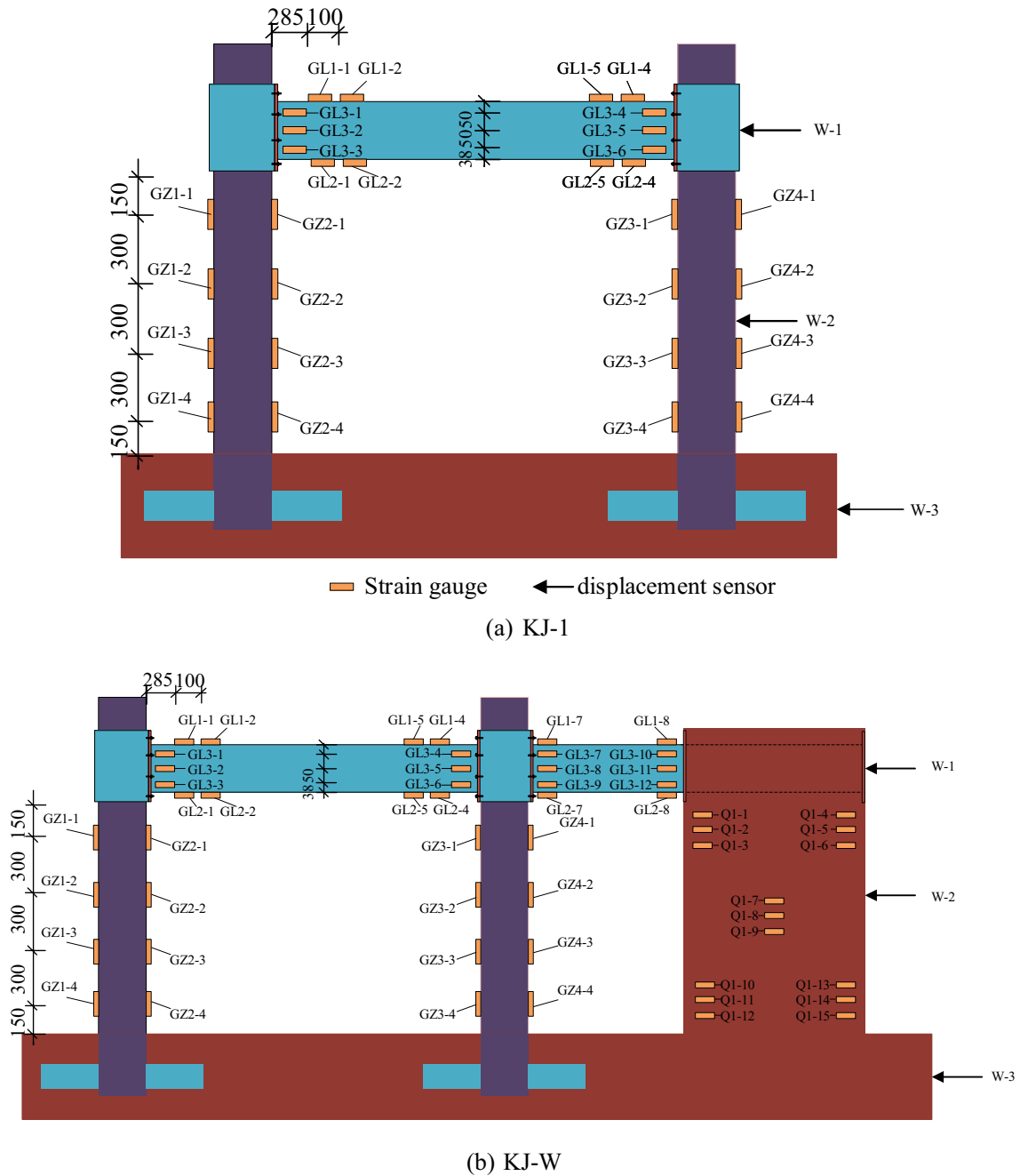


Fig. 11 Arrangement of strain gauges and displacement sensors

stiffness degradation is not obvious. With the increase in loading times, the intersection of the curves and the horizontal axis moved outward gradually, which meant the residual deformation is gradually significant. At the same time, the slope of the hysteresis curves decreased, indicating that stiffness degradation and accumulated damage occurred in the specimens.

Skeleton curve is the peak track of each cycle on hysteric curve. With the help of skeleton curve, the peak point,

limit point and yield point of each specimen can be obtained [31]. The characteristic points of each skeleton curve are listed in Table 4. In the elastic stage, When the specimens are loaded to 40–50% of the peak load, they are in the elastic stage, and the skeleton curve tended to be linear. The initial stiffness of the KJ-W specimen in the elastic stage is 1.6 times that of the KJ-1 specimen, indicating that the shell wall is increased the initial stiffness. After entering the plastic stage, the skeleton curves of the specimens are



Fig. 12 The failure mode of the column under different horizontal drifts of the KJ-1

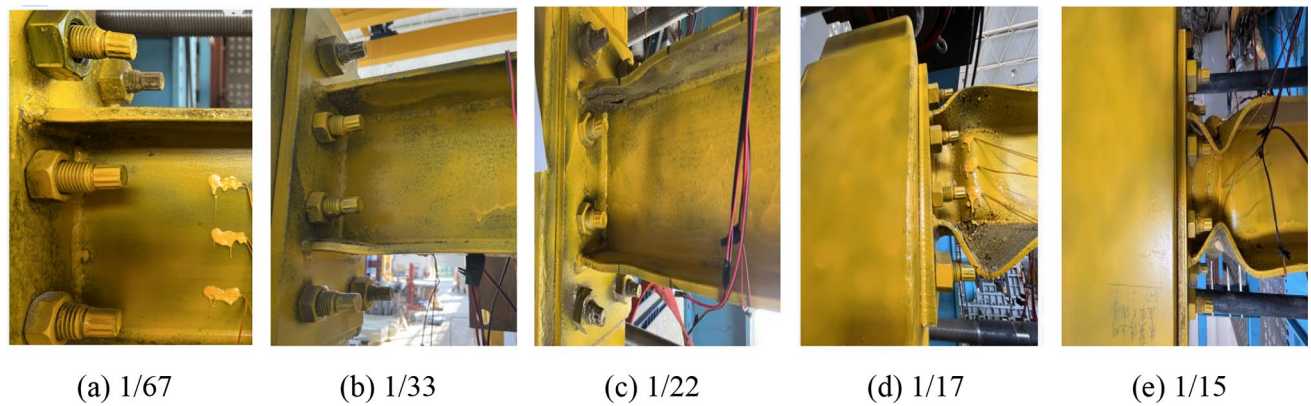


Fig. 13 The failure mode of steel beam joints under different horizontal drifts the KJ-1



Fig. 14 The failure mode of the column different horizontal drifts of the KJ-W



Fig. 15 The failure mode of steel beam joints under different horizontal drifts of the KJ-W

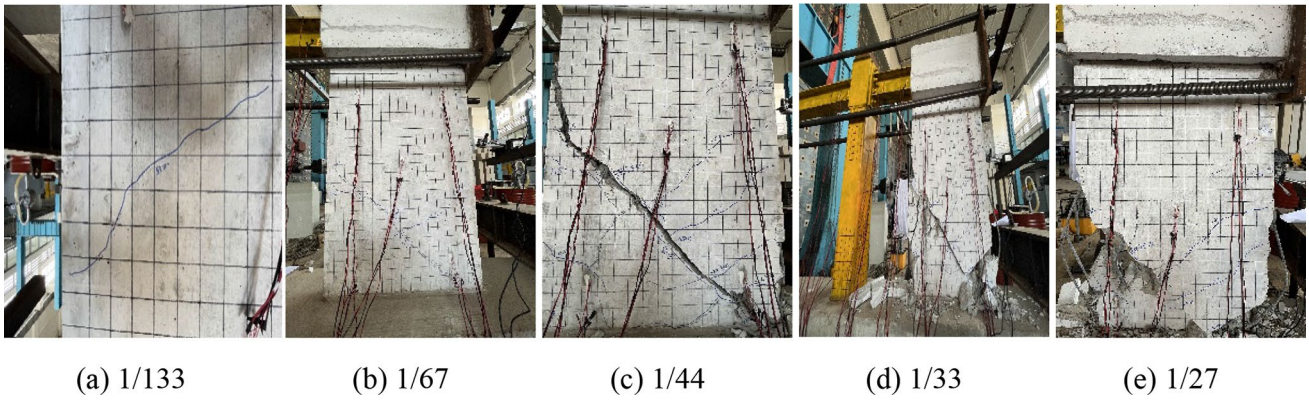


Fig. 16 The failure mode of the shear wall under different horizontal drifts of the KJ-W

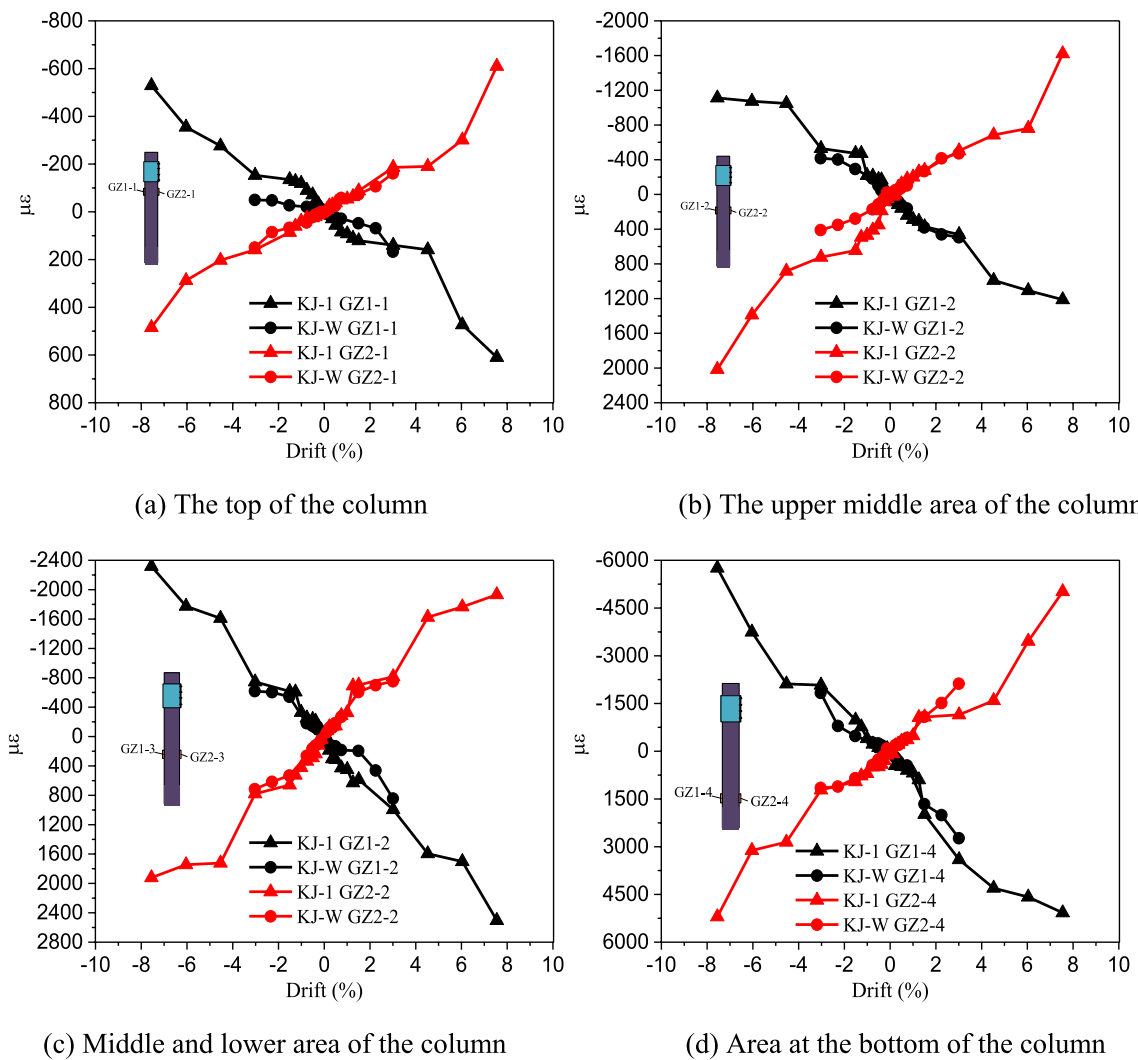


Fig. 17 Strain of the steel tube column with RAC infilled profile steel (the left column)

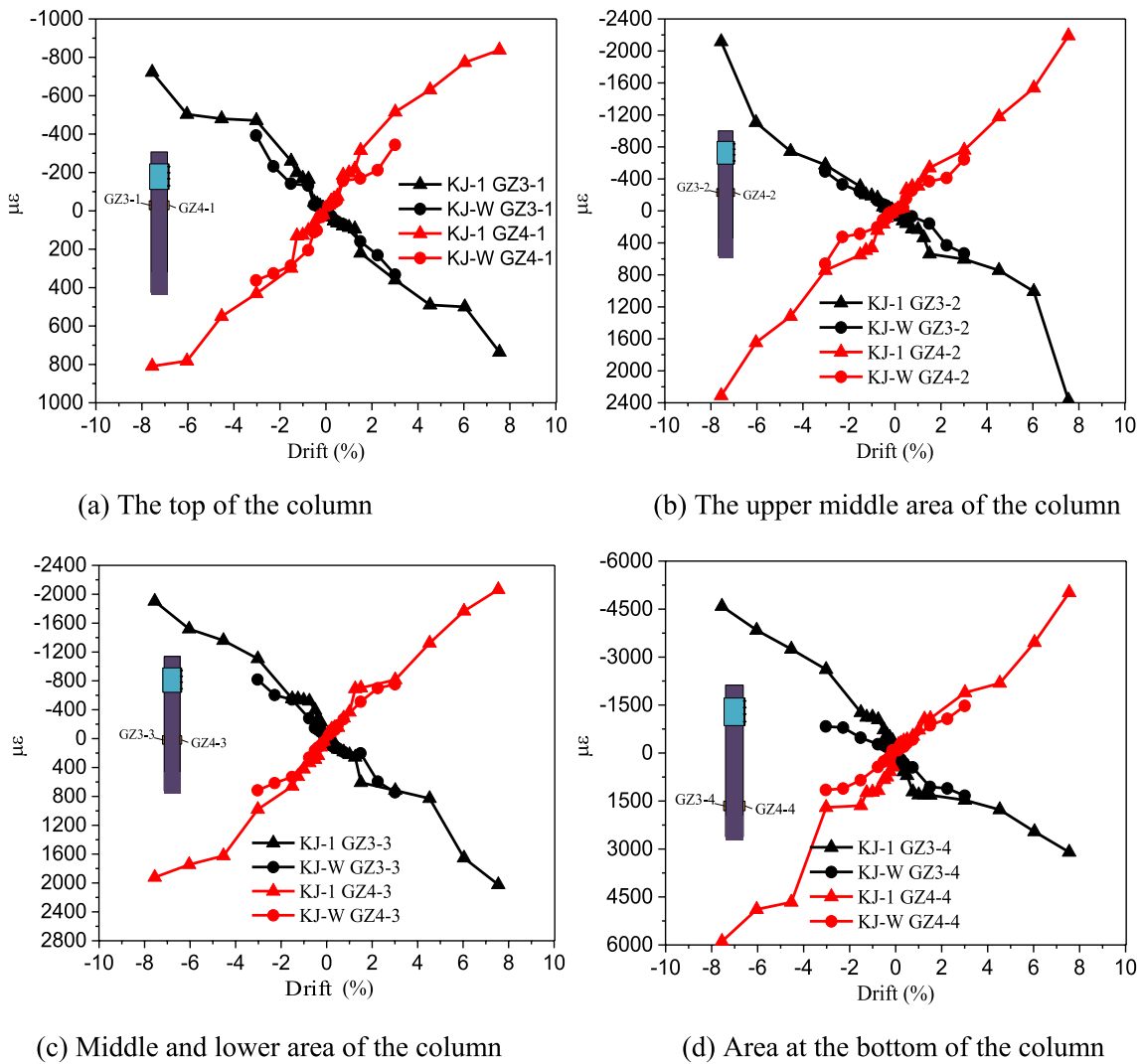


Fig. 18 Strain of the steel tube column with RAC infilled profile steel (the right column)

slightly separated. Among them, the peak bearing capacity of KJ-W is 15.2% higher than that of KJ-1, indicating that both the steel tube column with RAC infilled profile steel, the H-shaped steel beam and reinforced concrete shear wall exhibited good load capacity.

### 3.4 Ductility

Ductility is an important indicator to measure deformability. The ductility coefficient  $\mu$  of the KJ-1 and the KJ-W should be calculated by the following equation.

$$\mu = \frac{\Delta_u}{\Delta_y} \tag{1}$$

where  $\Delta_u$  is the displacement of the limit point, and  $\Delta_y$  is the displacement of the yield point.

It could be obtained from Table 3 that the ductility coefficient of the specimens varied from 1.38 to 1.49, indicating the KJ-W had good deformation performance. In addition, the ductility coefficient of the KJ-W increased by 7.4% compared with the KJ-1, indicating the shear wall improved the ductility. The yield and failure of the frame with reinforced concrete shear wall mainly appear in the shear wall, while those of the frame mainly appear in the steel tube columns with RAC infilled profile steel, and the H-shaped steel beams connecting the columns.

### 3.5 Strength and stiffness degradation

When the strength of the specimen degrades to a constant displacement, the bearing capacity decreases with the increase in loading times [32], and  $\lambda_i$  is the bearing capacity degradation coefficient of each level of loading, which is calculated as:

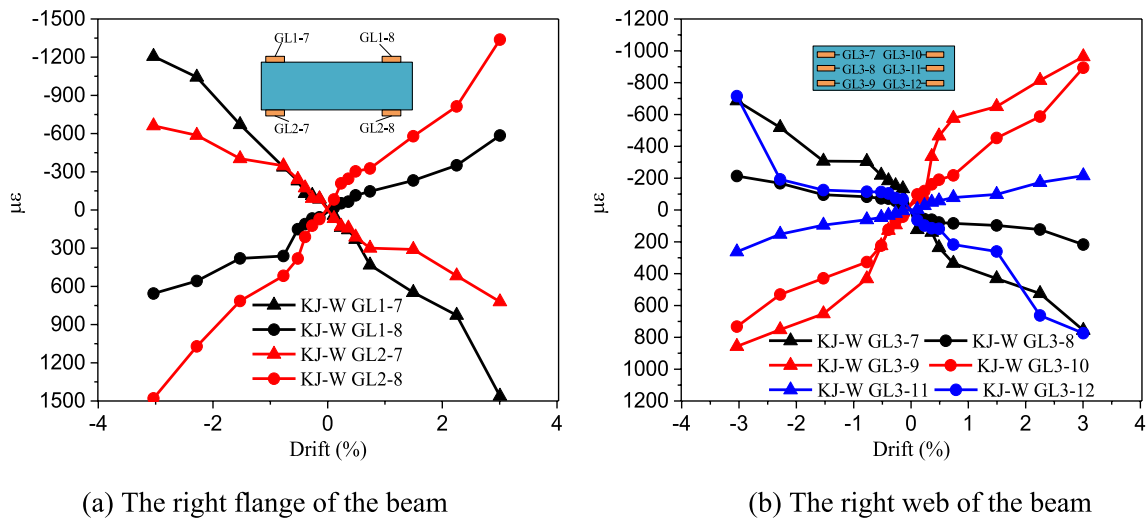


Fig. 19 Strain of the steel beam between the columns and the shear walls

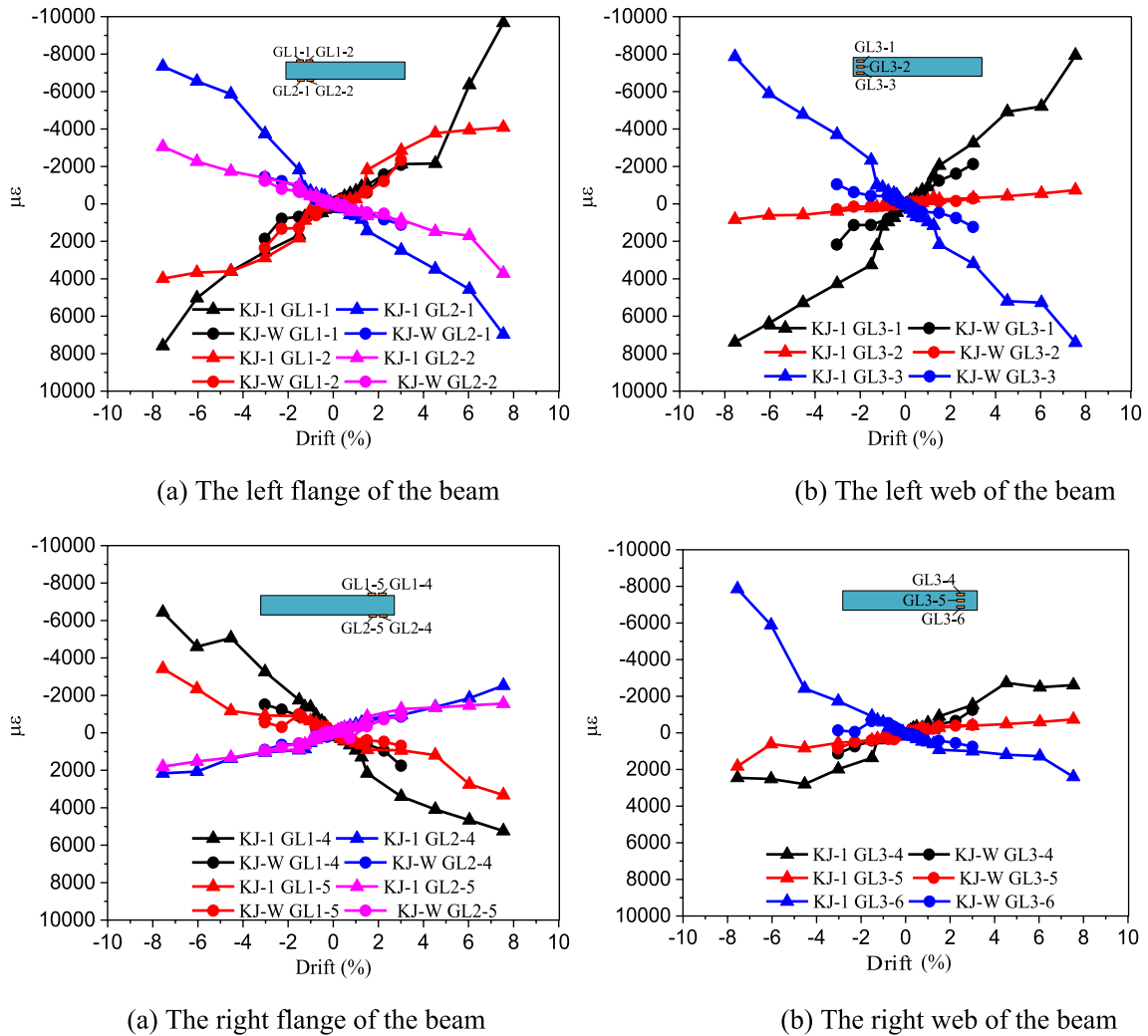


Fig. 20 Strain of the H-shaped steel beam between the two columns

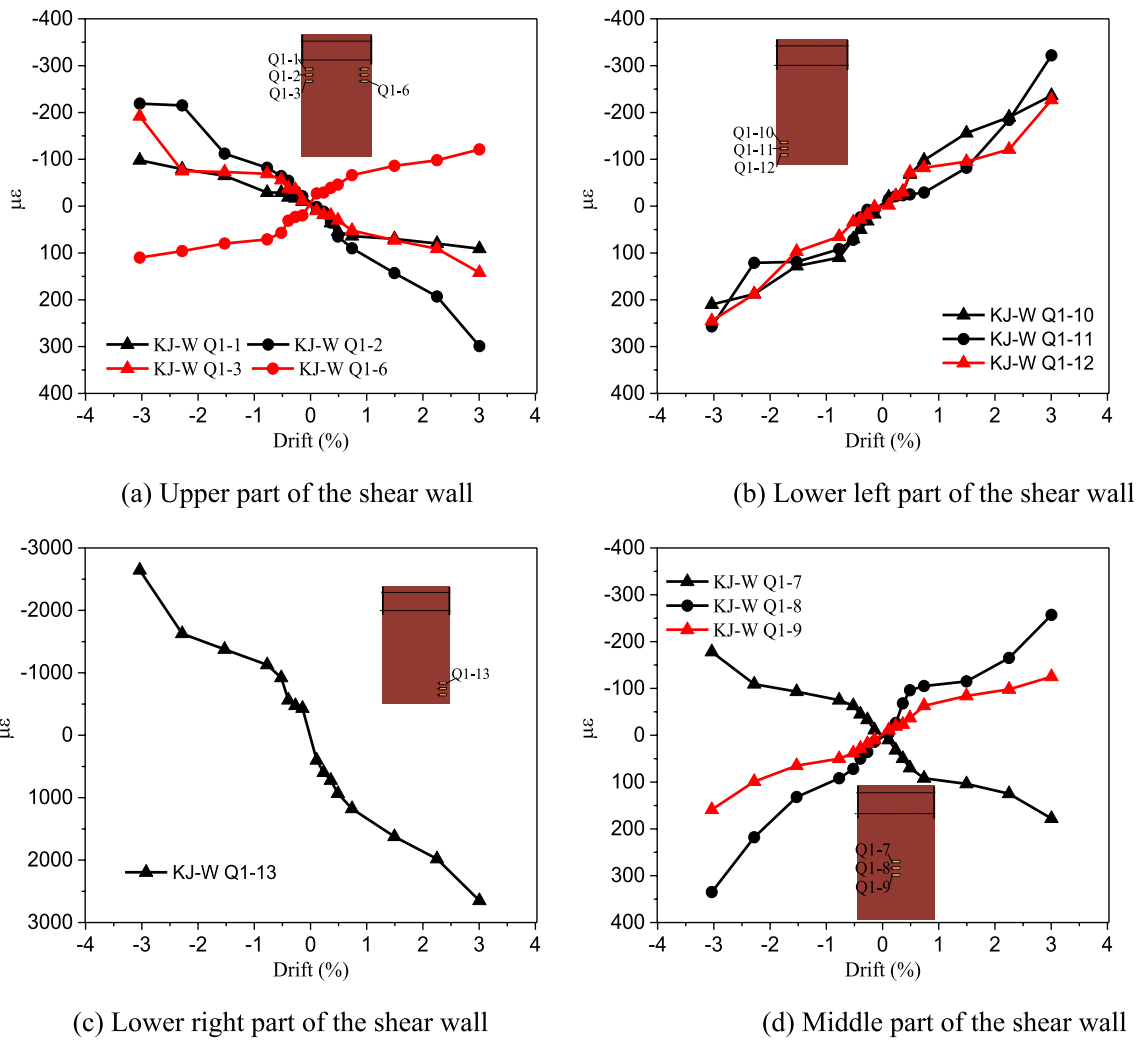


Fig. 21 Strain of the reinforced concrete shear wall

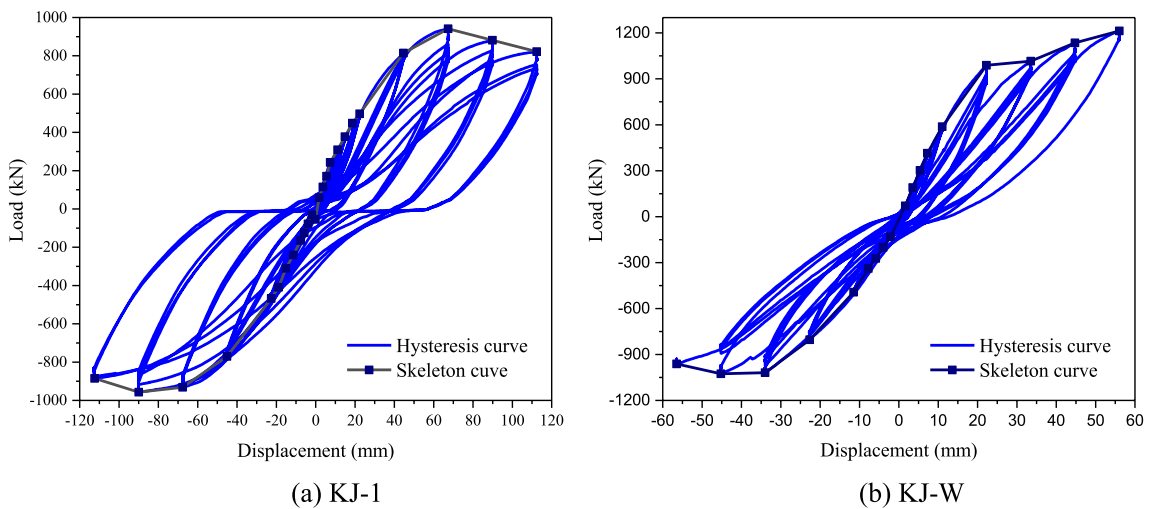
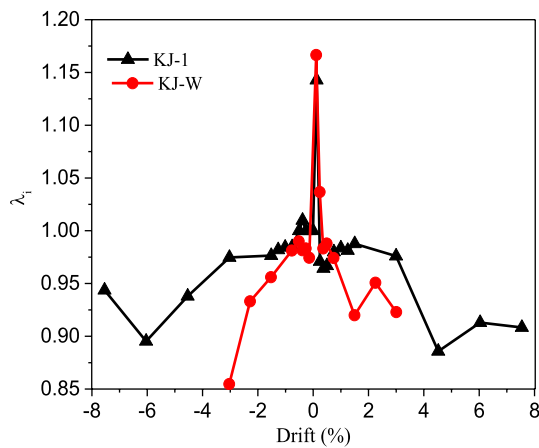


Fig. 22 Hysteresis curve and skeleton curves of specimens

**Table 4** Comparison of the results of the specimens

Specimen	Data sources	Yield point		Peak point		Limit point		Initial stiffness (kN/mm)	Ductility coefficient
		Load (kN)	Displacement (mm)	Load (kN)	Displacement (mm)	Load (kN)	Displacement (mm)		
KJ-1	Forward	842.8	49.8	941.1	67.4	821.5	112.4	16.9	1.38
	Reverse	860.8	64.4	957	90	885	112.4	13.4	
	Average	851.8	57.1	949.1	78.7	853.25	112.4	14.9	
KJ-W	Forward	1003.1	28.2	1212.9	56	1212.9	56	35.6	1.49
	Reverse	614.6	39.8	1025.9	45.2	961.9	56.5	15.4	
	Average	808.9	34	1119.4	50.6	1087.4	56.3	23.8	



**Fig. 23** Bearing capacity degradation coefficient curve

$$\lambda_i = \frac{P_i^j}{P_i^1} \tag{2}$$

where  $P$  is the peak load of the first cycle under the  $i$ -level displacement loading, and  $P$  is the peak load of the  $j$ -th cycle under the  $i$ -level displacement loading.

The stiffness degradation of the specimen is represented the secant stiffness, and its calculation formula is as follows:

$$K_i = \frac{\sum_{j=1}^n P_i^j}{\sum_{j=1}^n u_i^j} \tag{3}$$

where  $K_i$  is the displacement value corresponding to the peak load during the  $j$ -th cycle under the  $i$ -th level of displacement loading, and  $n$  is the number of cycles.

Figure 23 is the average value of forward and reverse direction capacity degradation coefficient after three cyclic displacement loadings. Overall, the strength degradation coefficient of each specimen is distributed between 0.85 and 1.18. The initial curve is relatively flat, indicating that the strength degradation at initial loading was not obvious. In the failure stage, the strength decreased more rapidly. During

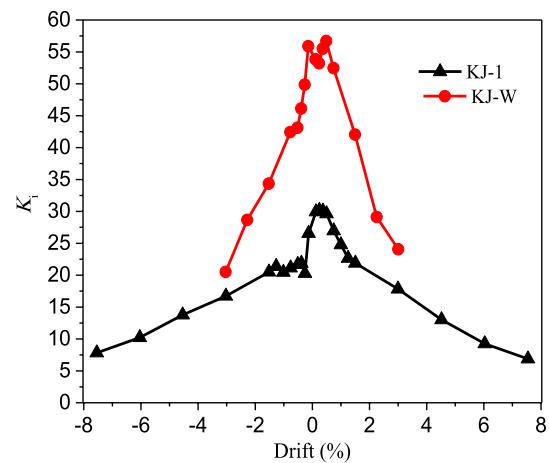


**Fig. 24** Stiffness degradation coefficient curve

the same drift process, the degradation coefficient of load-bearing capacity for the KJ-W is smaller than the KJ-1, indicating that the load-bearing capacity of the KJ-W decreases faster than the KJ-1. This suggests that the reinforced concrete shear wall has a certain influence on the load-bearing capacity degradation of the structure.

The stiffness degradation curves of specimens are shown in Fig. 24, which have the same trend. As the drifts increased, the stiffness decreased continuously. The initial stiffness of the KJ-W is greater than the KJ-1. With the increase in drift, the KJ-W exhibits a faster and more significant decrease in stiffness, whereas the stiffness degradation of the KJ-1 is slower. This indicates that the KJ-W experiences a deterioration in its cooperative performance with the frame after the cracking of the reinforced concrete shear wall. In contrast, the steel tube columns with RAC infilled profile steel of the KJ-1 effectively resist horizontal loads, ensuring a smoother degradation of stiffness in the specimen.

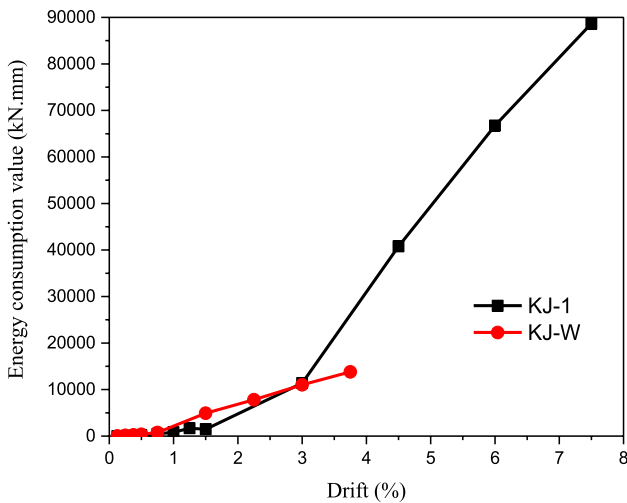


Fig. 25 Curve of energy consumption value

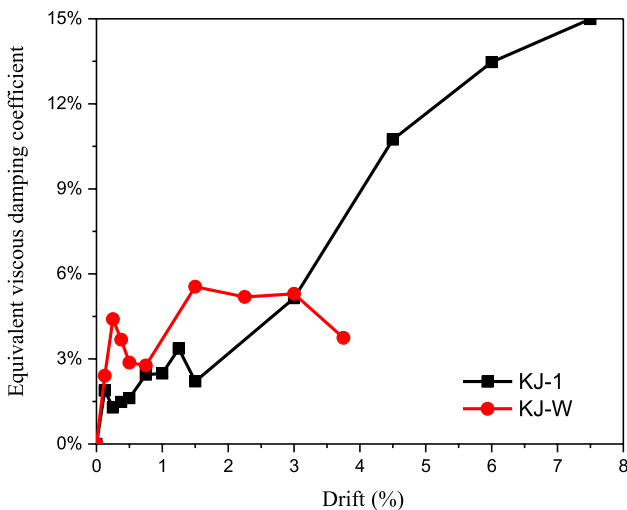


Fig. 26 Equivalent viscous damping coefficient

### 3.6 Energy consumption capacity

The accumulated energy consumption and equivalent viscous damping coefficient are used to evaluate the energy consumption capacity of the specimens and the calculated values are from reference [33]. The equivalent viscous damping coefficient curve and accumulated energy consumption of the specimens are presented in Figs. 25 and 26 respectively.

The energy dissipation in the specimens increases with the drift increase. Prior to reaching the yield point, the energy dissipation is decrease with the horizontal load decrease. As the specimens transition from the yield stage to the failure stage, the energy dissipation increases rapidly, indicating that

the primary energy dissipation phase in the specimens occurs from the yield stage to the failure stage.

The trend of the equivalent viscous damping coefficient with increasing drift shows an initial increase, followed by a decrease and then, another increase. For the KJ-W, during the elastic and yield stage, i.e., when the drift is less than 3%, the energy dissipation and equivalent viscous damping coefficient are greater than the KJ-1, indicates that the KJ-W exhibits better energy dissipation performance than the KJ-1. However, when the drift exceeds 3%, the KJ-W enters the failure stage, and at this point, the reinforced concrete shear wall experiences severe damage, resulting in lower energy dissipation capacity compared to the KJ-1.

## 4 Establishment and verification of FEM

The three-dimensional FEMs are established by ABAQUS software. The simulation of reciprocating loads on beam and column is using B31 beam elements, which have higher accuracy and better computational efficiency compared to solid elements [34, 35]. For this reason, B31 beam elements are more advantageous than solid elements in establishing the overall structure and calculating the response under seismic loads in the future research. S4R shell elements to simulate the nonlinear behavior of concrete shear walls. The H-shaped steels and square steel tubes of RAC columns are discretized in the form of \* rebar. The FEM is shown in Fig. 27.

### 4.1 Materials

The values of  $f_c$ ,  $f_t$  and  $E_c$  of RAC and ordinary concrete adopted the material-test values as listed in Table 3. The constitutive model provided by the GB50010-2010 [24] is commonly applied for plain concrete. The strain–stress relationship of unconfined concrete constitutive model under uniaxial tensile and compressive loading was as the following:

Under uniaxial compressive loading:  $y$

$$y = \begin{cases} ax + (3 - 2a)x^2 + (a - 2)x^3 & 0 < x \leq 1 \\ \frac{x}{b(x-1)^2+x} & x > 1 \end{cases} \quad (4)$$

where  $x = \epsilon/\epsilon_c$ ,  $y = \sigma/f_c$ ;  $a$  is the coefficient of the increasing stage of uniaxial compressive curve and could be calculated by  $a = 0.93 + 1.6e^{-1/26.46}$ ;  $\epsilon_c$  is the strain corresponding to the  $f_c$ ;  $b$  is the coefficient of the decreasing stage of uniaxial compressive curve and could be calculated by  $b = 1/(1.07 + 0.75e^{-1/13.76})$ .

Under uniaxial tensile loading :  $y = \begin{cases} 1.2x - 0.2x^6 & 0 < x \leq 1 \\ \frac{x}{a_t(x-1)^{1.7+x}} & x > 1 \end{cases} \quad (5)$



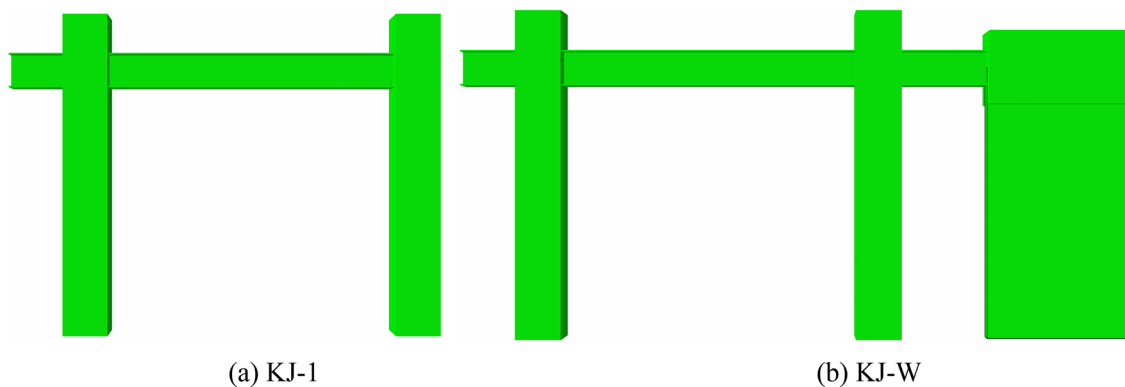


Fig. 27 Finite element model

where  $x = \epsilon/\epsilon_t$ ,  $y = \sigma/f_t$ ;  $a_t$  could be calculated by  $a_t = 0.312f_t^2$ ;  $\epsilon_t$  is the strain corresponding to the  $f_t$ ;

For confined concrete, the constitutive model provided by Wang [36] and Han [37]; the relationship between the uniaxial stress ( $\sigma$ ) and strain ( $\epsilon$ ) is as the following:

$$\sigma = \begin{cases} f_c' \frac{k(\frac{\epsilon}{\epsilon_0})}{k-1+(\epsilon-\epsilon_0)^k} & \epsilon \leq \epsilon_0 \\ f_c' - E_{des}(\epsilon - \epsilon_0) & \epsilon > \epsilon_0 \end{cases} \quad (6)$$

where  $f_c'$  is the concrete cylinder compressive strength.  $k = \frac{E_c}{E_c - (f_c')}$ ;  $\epsilon_0 = 0.00245 + 0.0122 \frac{\rho_v f_{yv}}{f_c'}$ ;  $\rho_v$  is the volumetric stirrup ratio;  $E_{des} = \frac{0.15f_c'}{\epsilon_c - \epsilon_0}$ ;  $\epsilon_{0.85} = 0.225\rho_v \sqrt{\frac{B_c}{s}} + \epsilon_0$ ;  $B_c$  and  $s$  are the sectional width of confined concrete and the stirrup space respectively.

The concrete damage plastic model (CDP model) [38] is applied to simulate the constitutive concrete. The isotropic tensile and compression molding are adopted to simulate the nonlinear behavior of the concrete. The dilation angle is taken as 30. The eccentricity is taken as 0.1. The value of  $f_{b0}/f_{c0}$  was taken as 1.16. The value of  $K_c$  was taken as 0.6667. The viscosity parameter is taken as 0.005. The relationship between  $\sigma_c(\sigma_t)$  and  $\epsilon$  followed Eq. (7):

$$\sigma = (1 - d)E_c \epsilon \quad (7)$$

where  $d$  is a variable of stiffness degradation, which can be calculated by theory of equivalent complementary energy assuming the damaged complementary energy.

$$d_c = 1 - \sqrt{\frac{\sigma_c}{E_c \epsilon_c}} \quad d_t = 1 - \sqrt{\frac{\sigma_t}{E_c \epsilon_t}} \quad (8)$$

Besides, the reduced elastic modulus  $E$  can also be defined from Fig. 3 with the following expression:

$$E = \frac{\sigma}{\epsilon - \epsilon^{pl}} \quad (9)$$

where  $\epsilon^{pl}$  is the concrete plastic strain:

$$\epsilon_c^{pl} = \epsilon_c - \frac{\sigma_c}{(1 - d_c)E_c} \quad \epsilon_t^{pl} = \epsilon_t - \frac{\sigma_t}{(1 - d_t)E_c} \quad (10)$$

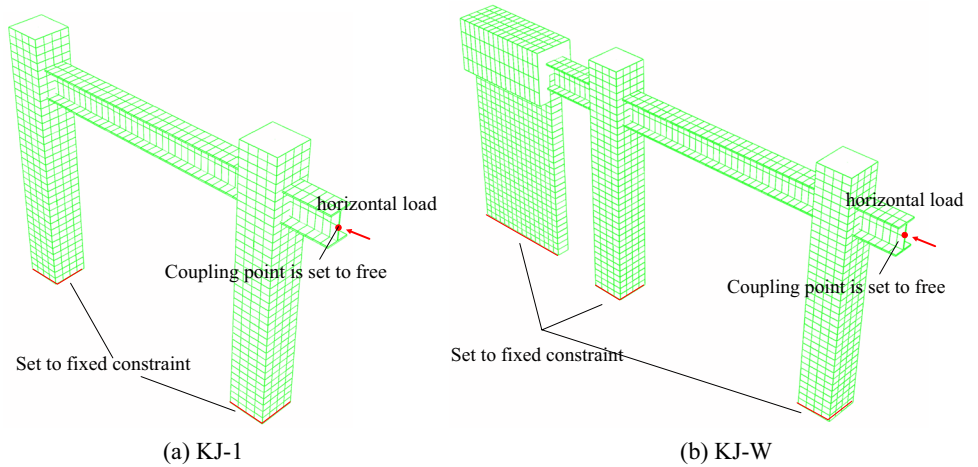
The multiple linear kinematic hardening model is employed to simulate steel in the FEM. The Poisson ratio is taken as 0.3. The steel skeleton and the load unload hysteresis model adopt the maximum point pointing model proposed by Clough [39].  $f_y$  and  $f_u$  were the yield strength and tensile strength of the steel respectively, which adopted the material-test values listed in Table 2.  $E_s$  is the elastic modulus of the steel and  $\alpha$  was taken as 0.01 after entering the strengthening stage. The Poisson's ratio of steel was 0.3. ABAQUS gives users the ability to define their constitutive material model using the subroutines interface UMAT. According to this study, the steel uniaxial material models are implemented into the UMAT subroutine using the FORTRAN programming language. The  $\sigma$ - $\epsilon$  relationship in the initial unidirectional loading stage could be described by the following equation.

$$\epsilon = \begin{cases} f/E_s & f \leq f_y \\ \frac{f_y}{E_s} + \frac{f-f_y}{\alpha E_s} & f \in (f_y, f_u] \end{cases} \quad (11)$$

### 4.2 Boundary conditions

The boundary conditions of the FEM were set according to the actual conditions, as shown in Fig. 28. The boundary constraint is applied by determining the end column and the shell wall. The loading point only released the freedom of horizontal and the rotational degrees about the horizontal. The merging nodes connection is set up between the beams and the columns, as well as between the beam and the shear wall.

Fig. 28 Boundary conditions



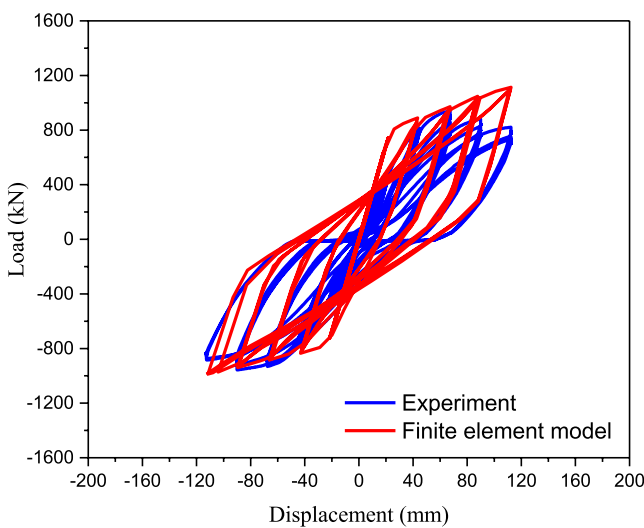
**4.3 Element mesh**

The global mesh size for the B31 element and the S4R element is taken as 50 mm to obtain enough accuracy of calculation. For the S4R element of concrete, the global mesh is set as 50 mm, since this size provided considerable accuracy among (30 mm, 50 mm, 70 mm, 100 mm, 200 mm) while assuring relatively rapid convergence, and the increase in concrete grid density severely increased the calculation time but brought limited promotion for calculation accuracy.

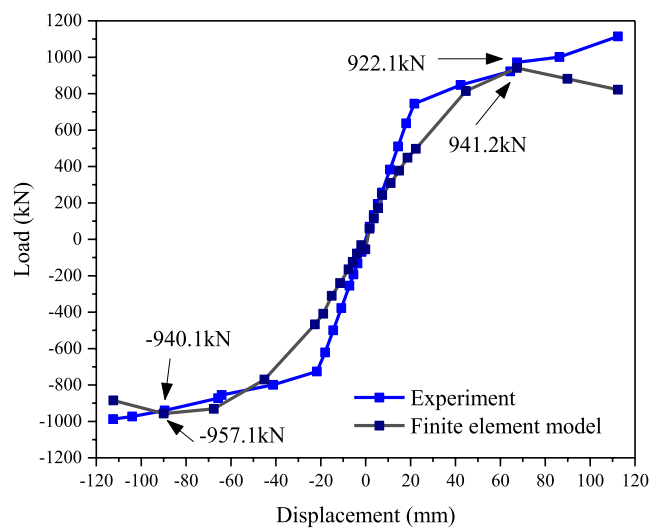
**4.4 Comparison of hysteretic curves**

The comparison the hysteresis curves and skeleton curves between the experiments and numerical simulations of each specimen is presented in Figs. 29 and 30. For the

KJ-1 specimen, the peak bearing capacity of the experiment is 941.2 kN and  $-957.1$  kN, and the finite element model has a bearing capacity of 922.1 kN and  $-940.1$  kN at the same displacement, with a difference of about 5%. For the KJ-W specimen, the peak bearing capacity is 1212.9 kN and  $-1025.9$  kN, and the finite element model had a bearing capacity of 1261.6 kN and  $-1388$  kN at the same displacement. The difference in forward bearing capacity is about 4%, and the difference in reverse bearing capacity was 35.3%. The large difference due to the sliding of the KJ-W specimen during the loading process, resulting in a lower reverse bearing capacity. The numerical simulation results of the two specimens coincide with the initial stiffness, peak bearing capacity, and skeleton curve of the experiment results, indicating that the finite element



(a) Hysteresis curves



(b) Skeleton curves

Fig. 29 The KJ-1 specimen

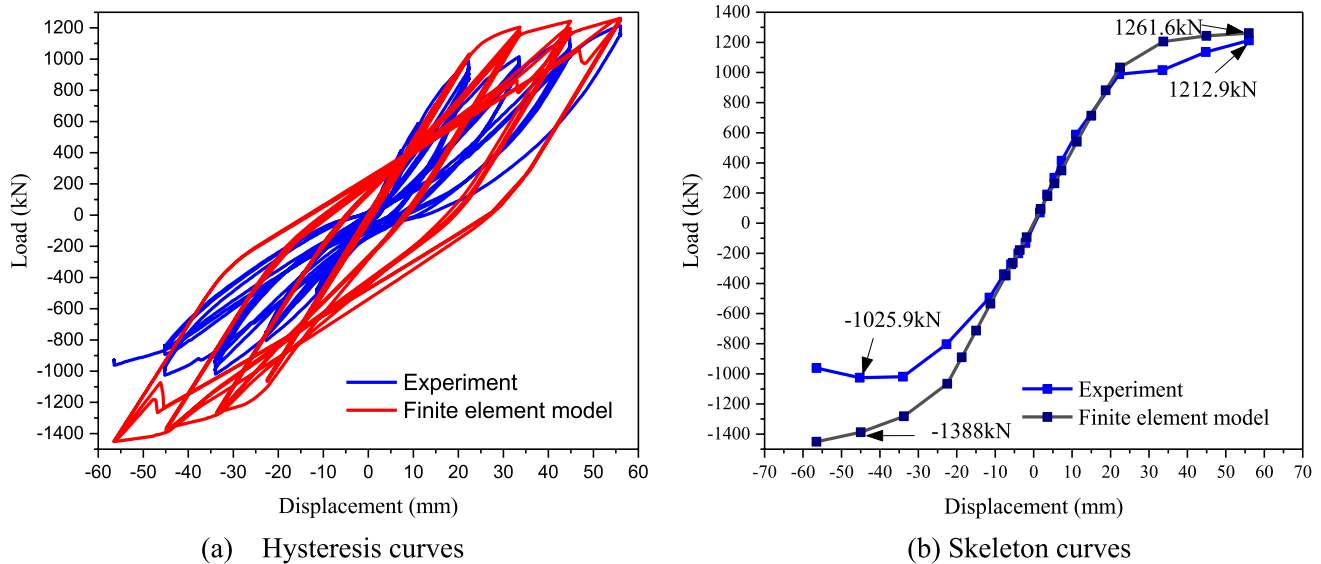


**Fig. 30** The KJ-W specimen

model established in this paper fairly reflect the hysteresis performance of the specimens.

#### 4.5 Comparison of typical phenomena

The damage of the FEM model is mainly concentrated in the position of the bottom of column, as shown in Fig. 31a. It could be found that the severe deformation is at the bottom of the experiment KJ-1 specimens, which is consistent with the FEM. The comparison result of the failure mode of the junction of the H-shaped steel beam and the steel tube column with RAC infilled profile steel, is presented in Fig. 31a. From the Mises stress cloud diagram, it could be observed that the stress at the junction had reached 491.2 MPa, which is the ultimate strength of the steel. The area with the greatest stress is distributed in the junction of the H-shaped steel beam and the steel tube column with RAC infilled profile steel, and the junction showed a typical stress concentration phenomenon, which was consistent with the failure mode in the experiment.

Figure 31b showed the DAMAGEC distribution of the concrete of shell wall at the ultimate state of the KJ-W. It could be found that the severely damaged parts of the concrete appear at the corners of the shear wall, forming an X-shape, this was quite consistent with the observations during the experiment. Figure 31b showed the stress distribution of the frame, it is found that the stress concentrated on the junction of the H-shaped steel beam and the steel tube column with RAC infilled profile steel obviously, which was also consistent with the concave in the photograph. The comparison result of the failure mode of the concrete is shown in Fig. 31b. In the experiment, the concrete at the

bottom of the column is severely damage. The damage factor, which could reflect the damage of the concrete in the FEM, reached 0.982, indicating that the failure mode of the core concrete was consistent with the experiment. It could be found that the results were in good agreement. The above viewpoints all reflected the feasibility of FEM, which verified that the FEM is correct.

## 5 Conclusion

The horizontal reciprocating loading experiments on two kinds of the RAC structure are investigated in the manuscript. Through the experiment and FEM verification, the following conclusions can be drawn:

1. The failure process and the failure pattern of the KJ-1 is the junction of the H-shaped steel beam, and the steel tube column with RAC infilled profile steel and the bottom of the column is damaged seriously. For the KJ-W, the reinforced concrete shear wall is damaged severely.
2. The peak bearing capacity of KJ-W is 15.2% higher than that of KJ-1, indicating that both the steel tube column with RAC infilled profile steel, the H-shaped steel beam and reinforced concrete shear wall exhibited good load capacity.
3. The ductility coefficient of the KJ-W increased by 7.4% compared with the KJ-1, indicating the shear wall improved the ductility. The yield and failure of the frame with reinforced concrete shear wall mainly appear in the shear wall, while those of the frame mainly appear in the

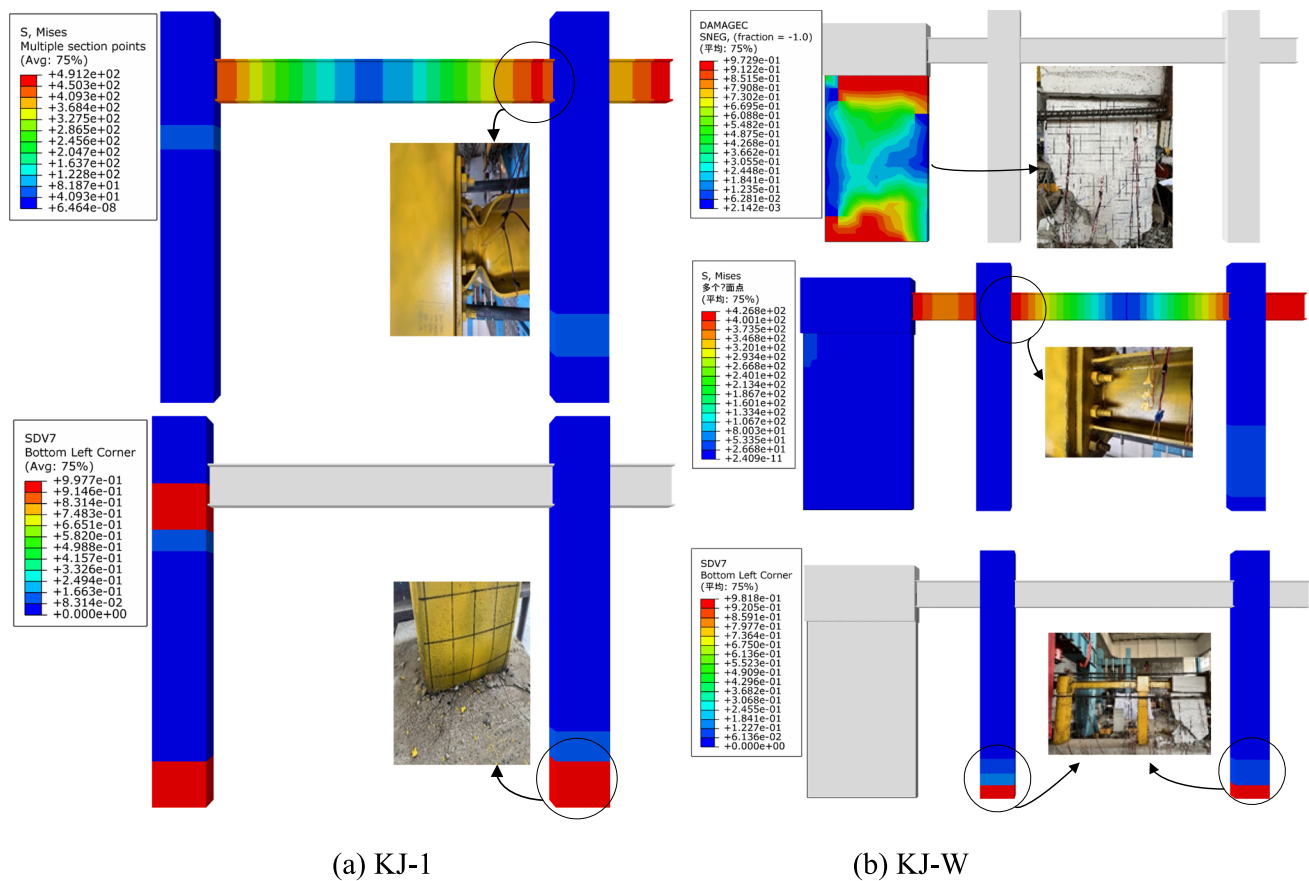


Fig. 31 Comparison of deformation between FEM and experiment results

steel tube columns with RAC infilled profile steel, and the H-shaped steel beams connecting the columns.

- During the same drift process, the degradation coefficient of load-bearing capacity for the KJ-W is smaller than the KJ-1, indicating that the load-bearing capacity of the KJ-W decreases faster than the KJ-1. This suggests that the reinforced concrete shear wall has a certain influence on the load-bearing capacity degradation of the structure.
- This manuscript investigates the seismic performance of RAC structural samples the KJ-1 and the KJ-W under horizontal reciprocating loading. There are not many types of structures, so they have certain limitations. Subsequent research can use multi story and multi span conduct dynamic time history analysis and small-scale structural seismic table simulation earthquake tests to accurately reflection the seismic performance of such structures under earthquake action.

**Acknowledgements** This project is supported by the National Natural Science Foundation of China (51678168).

## Declarations

**Conflict of interest** The author(s) declared no potential conflicts of interest with respect to the research, authorship and/or publication of this article.

## References

- Zaharieva R, Buyle-Bodin F, Wirquin E (2004) Frost resistance of recycle aggregate concrete. *Cem Concr Res* 34(10):1927–1932
- Júnior NSA, Silva GAO, Dias CMR (2019) Concrete containing recycled aggregates: estimated lifetime using chloride migration test. *Constr Build Mater* 222:108–118
- Sasanipour H, Aslani F, Taherinezhad J (2019) Effect of silica fume on durability of self-compacting concrete made with waste recycled concrete aggregates. *Constr Build Mater* 227:116598
- Kurda R, Silvestre JD, de Brito J (2018) Optimizing recycled concrete containing high volume of fly ash in terms of the embodied energy and chloride ion resistance. *J Clean Prod* 194:735–750
- Muduli R, Mukharjee BB (2020) Performance assessment of concrete incorporating recycled coarse aggregates and metakaolin: a systematic approach. *Constr Build Mater* 233:117223

6. Seyedhamed S, Kamal HK (2017) Restrained shrinkage cracking of recycled aggregate concrete. *Mater Struct* 50(4):1–15
7. Wang YY, Zhang H, Geng Y (2019) Prediction of the elastic modulus and the splitting tensile strength of concrete incorporating both fine and coarse recycled aggregate. *Constr Build Mater* 215:332–346
8. Gholampour A, Zheng J, Ozbakkaloglu T (2021) Development of waste-based concretes containing foundry sand, recycled fine aggregate, ground granulated blast furnace slag and fly ash. *Constr Build Mater* 267:121004
9. Wang DY, Lu CX, Zhu ZM, Zhang ZM, Zhang ZY, Liu SY, Ji YC, Xing ZQ (2023) Mechanical performance of recycled aggregate concrete in green civil engineering: review. *Case Stud Constr Mater* 19:e02384
10. Guo CY, Li XM, Zhang J, Lin JX (2023) A review on the influence of recycled plastic aggregate on the engineering properties of concrete. *J Build Eng* 17:107787
11. Lai ZC, Varma AH (2018) High-strength rectangular CFT members: database, modeling, and design of short columns. *J Struct Eng ASCE* 144(5):112–120
12. Ekmekyapar T, Hasan HG (2019) The influence of the inner steel tube on the compression behavior of the concrete filled double skin steel tube (CFDST) columns. *Mar Struct* 66:197–212
13. Ayough P, Sulong NH, Ramli IZ (2020) Analysis and review of concrete-filled double skin steel tubes under compression. *Thin-Walled Struct* 148–157
14. Shi YL, Xian W, Wang WD, Li HW (2020) Mechanical behavior of circular steel-reinforced concrete-filled steel tubular members under pure bending loads. *Structures* 25:8–23
15. Choi WC, Yun HD (2012) Compressive behavior of reinforced concrete columns with recycled aggregate under uniaxial loading. *Eng Struct* 41:285–293
16. Ma H, Dong J, Liu YH (2018) Compressive behavior of composite columns composed of RAC-filled circular steel tube and profile steel under axial loading. *J Constr Steel Res* 143(4):72–82
17. Bai G, Ma J, Liu B (2020) Study on the interfacial bond slip constitutive relation of I-section steel and fully recycled aggregate concrete. *Constr Build Mater* 238(3):117688
18. Muhammad JA, Maria I, Arslan A (2023) Performance of silica fume slurry treated recycled aggregate concrete reinforced with carbon fibers. *J Build Eng* 66(5):105892
19. Gholampour A, Gandomi AH, Ozbakkaloglu T (2017) New formulations for mechanical properties of recycled aggregate concrete using gene expression programming. *Constr Build Mater* 130(2):122–145
20. Hui M, Xue JY, Liu YH (2015) Cyclic loading tests and shears strength of steel reinforced recycled concrete short columns. *Eng Struct* 92(6):55–68
21. Pour AK, Shirkhani A, Zeng LL, Zhuge Y (2023) Experimental investigation of GFRP-RC beams with Polypropylene fibers and waste granite recycled aggregate. *Structure* 50:1021–1034
22. Pour AK, Shirkhani A, Kirgiz MS, Farsangi EN (2023) Influence of fiber type on the performance of reinforced concrete beams made of waste aggregates: experimental, numerical, and cost analyses. *Pract Period Struct Des Constr* 28(2):1–16
23. Pour AK, Shirkhani A, Kirgiz MS, Farsangi EN (2023) Experimental investigation of GFRP-reinforced concrete columns made with waste aggregates under concentric and eccentric loads. *Struct Concr* 24(1):1670–1688
24. China Architecture & Building Press (2010) GB50010–2010 Code for design of concrete structures. Beijing (**in Chinese**)
25. China Architecture & Building Press (2010) JGJ138–2016 Code for design of composite structures. Beijing (**in Chinese**)
26. China Standard Press (2011) GB/T 228.1–2010 Tensile test of metallic materials part 1: test method at room temperature. Beijing (**in Chinese**)
27. China Standard Press (2010) GB/T 25177–2010 Recycled coarse aggregates for concrete. Beijing. (**in Chinese**)
28. China Architecture & Building Press (2018) JGJ/T443–2018 Technical standards for recycled concrete structures. Beijing (**in Chinese**)
29. China Architecture & Building Press (2011) GB/T50081–2019 Codes for test methods of mechanical properties of ordinary concrete. Beijing (**in Chinese**)
30. China Architecture & Building Press (2015) JGJ/T 101–2015 Specification for seismic test of buildings. Beijing (**in Chinese**)
31. Chen Z, Dong S, Du Y (2021) Experimental study and numerical analysis on seismic performance of FRP confined high-strength rectangular concrete-filled steel tube columns. *Thin-Walled Struct* 162:107560
32. Esmaily A, Xiao Y (2005) Behavior of reinforced concrete columns under variable axial loads: analysis. *ACI Struct J* 102(5):736–744
33. Chen ZH, Chen JX, Du YS, Zhang YT, Zhen ZL, Liu YQ, Zhan LS (2023) Seismic behaviors of tailings and recycled aggregate concrete-filled steel tube columns. *Constr Build Mater* 365:130115
34. Maekawa K, Pimanmas A, Okamura H (2003) Nonlinear mechanics of reinforced concrete. Spon Press, London
35. Li Z, Hatzigeorgiou GD (2012) Seismic damage analysis of RC structures using fiber beam-column elements. *Soil Dyn Earthq Eng* 32:103–110
36. Wang WQ, Wang JF, Guo L, Guo X, Liu XX (2020) Behavior and analytical investigation of assembled connection between steel beam and concrete encased CFST column. *Structure* 24:562–579
37. Han LH, An YF (2014) Performance of concrete-encased CFST box stub columns under axial compression. *J Constr Steel Res* 93:62–76
38. Lee J, Fenves GL (1998) Plastic-damage model for cyclic loading of concrete structures. *J Eng Mech* 124(8):892–900
39. Clough RW, Johnston SB (1966) Effect of stiffness degradation on earthquake ductility requirements. Proceedings of Japan Earthquake Engineering Symposium, Tokyo, Japan.

**Publisher's Note** Springer Nature remains neutral with regard to jurisdictional claims in published maps and institutional affiliations.

Springer Nature or its licensor (e.g. a society or other partner) holds exclusive rights to this article under a publishing agreement with the author(s) or other rightsholder(s); author self-archiving of the accepted manuscript version of this article is solely governed by the terms of such publishing agreement and applicable law.